Biochemistry

Article

pubs.acs.org/biochemistry

Critical Role of Interdomain Interactions in the Conformational Change and Catalytic Mechanism of Endoplasmic Reticulum Aminopeptidase 1

Athanasios Stamogiannos,[†] Zachary Maben,[‡] Athanasios Papakyriakou,[†] Anastasia Mpakali,[†] Paraskevi Kokkala,[§] Dimitris Georgiadis,[§] Lawrence J. Stern,[‡] and Efstratios Stratikos*[,†]

[†]National Centre for Scientific Research Demokritos, Agia Paraskevi, 15341 Athens, Greece

[‡]Department of Pathology, University of Massachusetts Medical School, Worcester, Massachusetts 01655, United States

[§]Laboratory of Organic Chemistry, Department of Chemistry, University of Athens, Panepistimiopolis, Zografou, 15771 Athens, Greece

Supporting Information

ABSTRACT: Endoplasmic reticulum aminopeptidase 1 (ERAP1) is an intracellular enzyme that is important for the generation of antigenic epitopes and major histocompatibility class I-restricted adaptive immune responses. ERAP1 processes a vast variety of different peptides but still shows length and sequence selectivity, although the mechanism behind these properties is poorly understood. X-ray crystallographic analysis has revealed that ERAP1 can assume at least two distinct conformations in which C-terminal domain IV is either proximal or distal to active site domain II. To improve our understanding of the role of this conformational change in the catalytic mechanism of ERAP1, we used site-directed mutagenesis to perturb key salt bridges between domains II and IV. Enzymatic analysis revealed that these mutations, although located away from the catalytic site, greatly reduce the catalytic efficiency and change the allosteric kinetic behavior. The variants were more efficiently activated by small peptides and bound a competitive inhibitor with weaker affinity and faster dissociation kinetics. Molecular dynamics analysis suggested that the mutations affect the conformational distribution of ERAP1, reducing the population of closed states. Small-angle X-ray scattering indicated that both the wild type and the ERAP1 variants are predominantly in an open conformational state in solution. Overall, our findings suggest that electrostatic interactions between domains II and IV in ERAP1 are crucial for driving a conformational change that regulates the structural integrity of the catalytic site. The extent of domain opening in ERAP1 probably underlies its specialization for antigenic peptide precursors and should be taken into account in inhibitor development efforts.

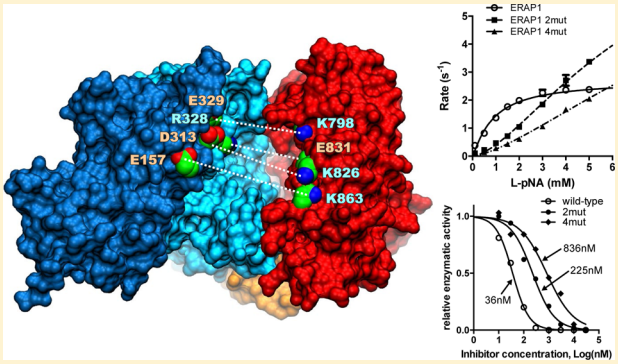

Endoplasmic reticulum aminopeptidase 1 (ERAP1) is an important enzyme for the function of the human immune system. ERAP1 generates peptides that bind to major histocompatibility class I (MHC-I) molecules and are then presented at the cell surface.[1] Through this function, ERAP1 can influence the cellular immunopeptidome and CD8-mediated T-cell responses against infected or malignant cells.[2] ERAP1 is normally localized in the endoplasmic reticulum (ER) but can also be secreted and play roles in the activation of innate immunity as well as blood-pressure regulation.[3,4] Over the past few years, ERAP1 has emerged as a pharmaceutical target for regulating adaptive immune responses with possible applications in cancer immunotherapy and the control of autoimmunity.[5,6]

ERAP1 belongs to the oxytocinase subfamily of M1 aminopeptidases, along with the homologous ER aminopeptidase 2 (ERAP2) and insulin-regulated aminopeptidase (IRAP), which also play roles in the generation of antigenic peptides.[7,8] ERAP1 is naturally polymorphic, and its allelic variants have been shown to associate with disease predisposition, primarily in autoimmunity, and to affect its trimming function.[9−11] Analysis of ERAP1 structure by X-ray crystallography revealed two distinct conformational states in which domains I and II are either in contact with, or distal to, domain IV of the enzyme.[12] These two conformations (termed "open" and "closed" states) affect the exposure of a large internal cavity to the external solvent. This cavity has been hypothesized to be the site of interaction with the peptide substrate and to facilitate peptide capture and catalysis.[13] Detailed comparison of the open and closed states has revealed key differences in the catalytic site: (a) Tyr438, a residue important for catalysis, is oriented away from the Zn(II) atom in the open state, and (b)

Received: November 17, 2016
Revised: January 20, 2017
Published: February 20, 2017

DOI: 10.1021/acs.biochem.6b01170
Biochemistry XXXX, XXX, XXX−XXX

residues 417−433, including key residues that form the S1 specificity pocket, are disordered in the open state. These observations have led to the hypothesis that the open state of ERAP1 is catalytically inactive and that the closed state is the catalytically competent conformation.[13,14] Furthermore, conventional as well as accelerated molecular dynamics simulations of ERAP1 suggested that the enzyme samples multiple open states in solution and is not limited to the conformations revealed by crystallographic analysis.[15] Whether a conformational change between the open and closed forms is a key component of the ERAP1 catalytic cycle in solution and how such a conformational rearrangement is linked to the catalytic site are however still unknown.

To gain insight into the importance of the catalytic mechanism of ERAP1 of the relative arrangement of domains I and II with respect to domain IV, we designed two ERAP1 variants in which key salt-bridge interactions between these domains are perturbed by site-directed mutagenesis. We combined enzymatic, computational, and small-angle X-ray scattering structural analysis to evaluate the functional and structural repercussions of these mutations. Overall, our findings indicate that interdomain interactions in ERAP1 are key to controlling the enzyme's solution structure as well as its conformational dynamics, and that they indirectly regulate the catalytic efficiency and mechanism of the enzyme. Our data provide novel insight into the mechanisms that underlie the specialization of this enzyme for antigenic peptide generation and also suggest a novel framework for designing potent inhibitors.

MATERIALS AND METHODS

Site-Directed Mutagenesis. Mutagenesis reactions to introduce the four mutations into ERAP1 (K828Q, E831Q, K798Q, and K863Q) were performed using the Quickchange II kit (Agilent Technologies), according to the manufacturer's instructions. Primers were designed with the Quickchange PrimerDesign tool (http://www.genomics.agilent.com) and were purified via high-performance liquid chromatography (HPLC). The sequences of primers were (5′−3′) as follows: K828Q FW, TGGAAACTCCTGAGTTTGTATTTTATCTCCCTTAAAGCTTTCATCTAG; K828Q REV, CTAGATGAAAGCTTTAAGGGAGATAAAATACAAACTCAGGAGTTTCCA; E831Q FW, AGTGTAAGAATTTGTGGAAACTGCTGAGTTTGTATTTTATCTCCC; E831Q REV, GGGAGATAAAATACAAACTCAGCAGTTTCCACAAATTCTTACACT; K798Q FW, TTTTCTTTGTCCAGTACTGAGCAAAGCCAAATTGAATTTGCCC; K798Q REV, GGGCAAATTCAATTTGGCTTTGCTCAGTACTGGACAAAGAAAA; K863Q FW, GAAAAACTGGAACAAACTTGTACAACAGTTTGAACTTGGCTCATCTT; K863Q REV, AAGATGAGCCAAGTTCAAACTGTTGTACAAGTTTGTTCCAGTTTTTC. The initial template was the pDEST8-ERAP1 plasmid containing the 528K, 730Q polymorphisms and a C-terminal His tag (generously donated by A. Hattori, Kyoto University, Kyoto, Japan). After each mutagenesis reaction, the selected mutation was verified by sequencing (VBC), and the purified plasmid was used as a template for the next reaction in the following order: K828Q → E831Q → K798Q → K863Q.

Recombinant Enzyme Production and Purification. pDEST8-ERAP1 plasmids were transformed into DH10Bac competent cells for transposition into the bacmid, according to the instructions for the Bac-to-Bac system (Invitrogen). White colonies containing the recombinant bacmid were selected for DNA isolation. One colony was selected and allowed to grow overnight, in Luria broth medium with the appropriate antibiotics (50 μg/mL kanamycin, 7 μg/mL gentamicin, and 10 μg/mL tetracycline). The next day, the culture was collected and centrifuged at 4000 rpm for 20 min. The cell pellet was resuspended in 100 mM Tris (pH 8.0), 8% sucrose, and 10 mM EDTA, in the presence of RNase A (100 μg/mL) and lysozyme (50 μg/mL), and the mixture was incubated at room temperature for 10 min. Cells were then lysed with 1% SDS in Tris-EDTA buffer, and after a 10 min incubation at 37 °C, potassium acetate (5 M) was added to the mixture. After centrifugation to remove the debris, the DNA in the supernatant was precipitated with isopropanol. The pellet was washed with 70% EtOH, air-dried, and resuspended in Tris-EDTA buffer (pH 8.0). The correct transposition was verified by PCR, according to the instructions for the Bac-to-Bac system.

The bacmid DNA was then transfected to insect Sf9 adherent cells, growing in SF900II serum-free medium (Life Technologies). For transfection, the Cellfectin reagent (Invitrogen) was used according to the manufacturer's instructions. Transfection was performed in six-well plates, and ∼4−5 μg of bacmid DNA was used per well. Cells were left to grow for 4−6 days in the presence of gentamicin (50 μg/mL). After that period, the culture was collected and centrifuged at 1250 rpm, and the virus was isolated and filtered from the cell supernatant. The virus was further amplified in Sf9 adherent cells (P1 virus stock) and then in Hi5 insect cells in suspension (P2 virus stock).

For protein production, Hi5 insect cells grown in SF900II serum-free medium (Invitrogen) were infected with a P2 baculovirus stock, and 3−4 days later, the cell medium was harvested by centrifugation. The cell supernatant was extensively dialyzed against a 10 mM phosphate buffer (pH 8.0) containing 100 mM NaCl. After dialysis, the composition of the supernatant was adjusted to 50 mM sodium phosphate (pH 8.0), 300 mM sodium chloride, and 10 mM imidazole, and the sample was mixed with Ni-NTA resin and allowed to bind while being weakly stirred for 2 h. The slurry was packed into a gravity column and washed. The protein was eluted using a 20 to 150 mM imidazole step gradient. The fractions collected were tested for aminopeptidase enzymatic activity, using as a substrate L-leucine 7-amido-4-methyl coumarin (L-AMC, Sigma), and the enzyme purity was validated via sodium dodecyl sulfate−polyacrylamide gel electrophoresis (SDS−PAGE). The enzyme-containing fractions were dialyzed against a 10 mM Hepes (pH 7.0), 100 mM NaCl buffer and stored as single-use aliquots with 10% glycerol at −80 °C. The proteins were quantified by SDS−PAGE densitometry, using ImageJ and known concentration standards.

Enzymatic Assays. The aminopeptidase activity of recombinant ERAP1 was measured by following the change in the fluorescent signal produced upon digestion of the substrate L-AMC (Sigma-Aldrich). The fluorescence was measured at 460 nm, whereas the excitation was set at 380 nm. Measurements were performed on a TECAN infiniteM200 microplate fluorescence reader and on a QuantaMaster 400 spectrofluorimeter (Photon Technology International, Birmingham, NJ). Enzymatic activity was also measured by following the change in the fluorescent signal produced upon excision of an internally quenched N-terminal tryptophan residue from the WRVYEKC^{DNP}ALK peptide.[16] These measurements were

DOI: 10.1021/acs.biochem.6b01170
Biochemistry XXXX, XXX, XXX−XXX

performed on a QuantaMaster 400 spectrofluorimeter (Photon Technology International), with excitation set at 295 nm and fluorescence measured at 350 nm.

Michaelis−Menten (MM) analysis was performed by measuring the rate of hydrolysis of the chromogenic substrate L-leucine-*p*-nitroanilide (L-pNA) for a series of substrate concentrations. The measurements were performed on a TECAN infinite M200 microplate fluorescence reader. Initial reaction rates were calculated for each concentration, and the data were fit to an allosteric (cooperative) sigmoid model, using GraphPad software, according to the equation $\gamma = (V_{max}X^h)/(K_{prime} + X^h)$, where X is the substrate concentration, Y the initial reaction rate, V_{max} the reaction rate at infinite time, and h the Hill slope. K_{prime} is a parameter related to K_M and is calculated with the equation $K_{prime} = K_{half}{}^h$, where K_{half} is the concentration of the substrate that produces a half-maximal enzyme velocity. For selecting between classical and allosteric MM models for fitting the data, the corrected Akaike's Information Criteria test was used (https://graphpad.com/quickcalcs/AIC1.cfm).

For analysis of the digestion of the LG_xL peptides, each peptide at 20 μM was incubated with 5 nM ($LG_{8-10}L$) or 50 nM ($LG_{3-7}L$) ERAP1, 30 nM ($LG_{8-10}L$) or 300 nM ($LG_{3-7}L$) ERAP1 2mut, and 50 nM ($LG_{8-10}L$) or 500 nM ($LG_{3-7}L$) ERAP1 4mut, at 37 °C for 1 h, in a 50 mM Hepes (pH 7.0), 100 mM NaCl buffer. Reactions were terminated via the addition of 0.25% (v/v) trifluoroacetic acid (TFA). The reactions were analyzed via reverse phase HPLC (chromolith C-18 column, Merck) by following the absorbance at 220 nm. A linear gradient elution system was used (solvent A, 0.05% TFA; solvent B, 0.05% TFA and 40% AcN). The percentage of substrate cleaved was calculated by integration of the area under each peptide peak, using appropriate standards. The specific activity was calculated using the GraphPad software, by fitting the results in the one-phase decay equation $Y = Y_O e^{-kx}$, where x is the reaction time, Y_0 the substrate fraction left intact after time zero (constrained as $Y = 1$), Y the substrate fraction left intact after the end of the reaction, and k the reaction rate constant.

For the inhibition assay, L-AMC fluorescence measurements were taken in a TECAN infinite M200 microplate fluorescence reader as stated above. Briefly, 5 nM ERAP1 was incubated with 200 μM L-AMC and various concentrations of ERAP1 inhibitor DG013A. The reaction was followed for 5−10 min, and activity was calculated by measuring the slope of the time course. For calculation of the *in vitro* IC_{50} values, experimental data were fit to the following equation using GraphPad Prism:

$$Y = \text{bottom} + \frac{\text{top} - \text{bottom}}{1 + 10^{(\log IC_{50} - X)\times \text{Hill slope}}}$$

where Y is the enzymatic activity, X is the inhibitor concentration, top and bottom are the maximum and minimum Y values in the graph, constrained as 1 and 0, respectively, and IC_{50} is the inhibitor concentration needed to acquire half-maximal enzyme activity.

For the kinetic association experiments, we employed L-AMC fluorescence measurements in a QuantaMaster 400 spectrofluorimeter equipped with an SFA-20 rapid kinetics accessory (Hi-Tech Scientific). Fluorescence emission was measured for up to 30 min, and the experimental data were fit to the following equation using GraphPad Prism:

$$[P] = V_s t + \frac{V_i - V_s}{k_{obs}}(1 - e^{-k_{obs}t})$$

where [P] is the concentration of the formed product and is analogous to the fluorescence signal measured, V_i is the initial reaction rate, V_s is the steady-state reaction rate (after enzyme−inhibitor equilibrium has been reached), and k_{obs} is the observed reaction rate constant. For faster reactions with limited data points that resulted in poor fits to that equation, a different approach was used. First, the change in the fluorescence signal over time was transformed to enzymatic reaction rate by calculating the first derivative of the experimental data. Data were smoothed using a Savitzky−Golay filter to reduce noise and were fit to the one-phase decay equation $Y = (Y_0 - \text{plateau})e^{-kx} + \text{plateau}$, where Y is the reaction rate, X the time, Y_0 the initial reaction rate, plateau the equilibrium reaction rate, and k the observed reaction rate constant.

For the kinetic dissociation experiments, ERAP1 wild-type (wt) and mutant enzymes were incubated with an excess of inhibitor (10-fold greater than the calculated IC_{50}) for 10 min at room temperature, to allow for the formation of enzyme−inhibitor complexes. Afterward, the mixture was diluted 100-fold in a 200 μM L-AMC buffer in a quartz cuvette, and the fluorescence emission was followed for 40 min at room temperature in a QuantaMaster 400 spectrofluorimeter, with the wavelengths specified above. The dead mixing time was 20 s. The change in fluorescence over time was transformed to enzymatic reaction rate by calculating the first derivative of the experimental data. Data were smoothed to reduce noise and fit with GraphPad Prism to the one-phase association equation $Y = Y_0 + (\text{plateau} - Y_0)(1 - e^{-kX})$, where Y is the reaction rate, X the time, Y_0 the reaction rate for time zero, plateau the reaction rate after equilibrium has been established, and k the observed reaction rate constant.

Computational Methods. Preparation of the Simulation Systems. The ligand-free enzyme models were based on the X-ray crystal structures of human ERAP1 complexes with bestatin, either in the closed state [Protein Data Bank (PDB) entry 2YD0][14] or in the three open states found in the asymmetric unit of PDB entry 3MDJ.[13] To prepare the simulation systems as closely as possible to the experimental constructs, proteins were modified according to the sequence of the ancestral ERAP1 (UniProt entry Q9NZ08), with the exception of Arg127 that was mutated to Pro. For the same reason, we added 13 N-terminal residues (33−45), the missing C-terminal residues 935−941, and a six-His tag (Figure S6). The inhibitor was replaced with a water molecule, and the maximal number of glycan residues that were resolved in the X-ray structures was retained, specifically, the branched five-sugar unit (N-acetyl-D-glucosamine)$_2$−β-D-mannose−(α-D-mannose)$_2$ linked at Asn70, a two-unit N-acetylglucosamine at Asn154, and a single N-acetylglucosamine sugar at Asn414 and Asn760. The quadruple mutant of the wt ERAP1 construct (4mut-ERAP1) was prepared by changing Lys798, Lys828, Glu831, and Lys863 to glutamine in the initial models (one closed and three open states). Addition of missing residues using MODELER (version 9.10)[17] and the setup of histidine protonation states using H++ (version 3.1)[18] were performed as described previously.[15] The simulation systems were prepared using the LEaP module of AMBER (version 14),[19] with the ff14SB force field for protein atoms,[20] the GLYCAM06j force field for sugars,[21] and a simple bonded

DOI: 10.1021/acs.biochem.6b01170
Biochemistry XXXX, XXX, XXX−XXX

representation for zinc.[22] Proteins were solvated in cuboid boxes comprising TIP3P[23] water molecules with a minimum distance of 9−10 Å between the protein and the edge of the periodic box (32025 and 35950 waters added in closed and open ERAP1, respectively). The total charge of the systems was neutralized by adding 12 K^+ ions, and then 116 Na^+ and Cl^- ions were added to approximate an ionic strength of 0.15 M. A description of the eight ERAP1 model systems employed for the MD simulations can be found in Table S1.

Conventional Molecular Dynamics Simulations. Conventional (cMD) and accelerated (aMD) molecular dynamics simulations were performed with the GPU version of PMEMD program using periodic boundary conditions.[24] A time step of 2.0 fs and the SHAKE algorithm were used to constrain the bonds connecting H atoms.[25] The temperature was controlled using a Langevin thermostat with a collision frequency of 2.0 ps^{-1},[26] and the pressure was regulated at 1 bar using the Berendsen weak-coupling algorithm with a relaxation time of 2.0 ps.[27] Electrostatic interactions were evaluated by means of the particle mesh Ewald method with a real space cutoff of 9.0 Å and a direct sum tolerance of 10^{-6}.[28] The center of mass of the solute was reset to zero every 1000 steps, and the reciprocal sum was calculated every single step.

Each system was first energy minimized to remove any close contacts, and then harmonic positional restraints (force constant of 50 kcal mol^{-1} $Å^{-2}$) were applied to the protein backbone atoms. The temperature was increased from 10 to 300 K as a linear function of time over the course of a 100 ps simulation under a constant volume (*NVT* ensemble). The restraints were gradually removed over nine rounds of 100 ps in the isothermal−isobaric (*NPT*) ensemble, and then an additional unrestrained simulation was performed for 9 ns under a constant pressure of 1 bar at 300 K. Production runs were performed for 500 ns in the *NPT* ensemble under the same conditions, but using the Monte Carlo barostat introduced in AMBER 14. An aggregate of 4 μs cMD simulations was acquired for the two ERAP1 constructs (wt and 4mut) starting from the closed state and three open states. Trajectory snapshots were collected every 1000 steps (2 ps) for further processing, excluding the initial 10 ns of the equilibration period.

With the aim of enhancing exploration of the conformational space, dual-boost aMD calculations (one boost potential only to the torsional terms and another separate boost potential to the total potential) were performed in the *NPT* ensemble with the same parameters as in the cMD simulations. Twenty independent dual-boost aMD calculations of 50×10^6 steps, which correspond to 100 ns, albeit with a time scale of aMD that is nonlinear and cannot be assessed accurately, were seeded from the cMD simulations of the three open ERAP1 states of both constructs, and four additional aMD simulations of 50×10^6 steps starting from the closed state of ERAP1 (Table S1). For the open ERAP1 states, we selected 10 cMD snapshots per construct at different interdomain angles in the θ range of 60−72°. Selection of the aMD boost parameters was based on previous work by the McCammon group,[29,30] and specifically, an average total potential energy and average torsional potential energy were computed from the equilibrated phase of the cMD simulations and used for the calculation of a common dual-boost potential employed in all aMD calculations. Total acceleration parameter α_{pot} was set equal to 0.16 kcal mol^{-1} × (total number of atoms) = 19650 kcal mol^{-1}, and torsional boost parameter α_{tor} = 0.8 kcal mol^{-1} × (number of solute residues) = 732 kcal mol^{-1}. As observed previously,[15] closed ERAP1 simulations sampled a very narrow range of interdomain angles and remained closed during the course of either cMD or aMD simulations even when higher-acceleration rounds of aMD simulations were performed by increasing the torsional boost potential threshold by α_{tor}. The bias potentials were collected every 1000 steps for both total and torsional boost, and then each frame was reweighted on the basis of a Maclaurin series expansion to the 10th order using the PyReweighting Python scripts.[31]

Trajectory processing, clustering, and principal component analysis were performed with the CPPTRAJ module of AmberTools (version 15)[32] after mass-weighted root-mean-square deviation (RMSD) fitting with respect to the domain III backbone (residues 530−614) of closed ERAP1. N-terminal residues 33−45, missing loop residues 486−514, and the C-terminal His tag were not included in the processing. Clustering of trajectories was performed using the hierarchical agglomerative approach with a minimum distance between clusters of 1.0, 1.5, or 2.0 Å, depending on the desired diversity of the resulting clusters. Interdomain angle θ was defined as the angle of the centers of mass of domains I and II (residues 46−529), domain III (residues 530−614), and domain IV (residues 615−940). Interdomain torsion angle φ was taken between the center of mass of domains I and II (residues 46−529), residues 577 and 612 (domain III), and the center of mass of domain IV (residues 615−940) backbone atoms. Visual inspection of the trajectories and rendering of the figures were performed with VMD (version 1.9).[33] Calculations were performed on a dual Intel Xeon server operated by Linux x86_64 kernel version 2.6.32 with CUDA 5.0 and equipped with quad NVIDIA GTX 780 GPUs.

Sample Preparation and SAXS Measurements. wt-ERAP1 and 4mut-ERAP1 sequences with a C-terminal six-His tag in pDEST8 were secreted from baculovirus-infected High Five cells and purified by NiNTA affinity chromatography, anion exchange chromatography, and size exclusion chromatography. Samples were concentrated to >5 mg/mL in rinsed centrifugal concentrators (molecular weight cutoff of 10 kDa), and buffer [50 mM HEPES (pH 7.5), 200 mM sodium chloride, 2% glycerol, and 0.02% sodium azide] was collected from the flow-through. Three serial dilutions of purified wt-ERAP1 (5.6, 2.8, and 1.4 mg/mL) and 4mut-ERAP1 (2.5, 4.9, and 9.8 mg/mL) were arrayed along with matched buffer, and scattering data were collected at beamline 12.3.1 of Lawrence Berkeley National Laboratory (Berkeley, CA) using 0.5 s, 1 s, 2 s, and two 4 s exposures. Images were radially averaged, and buffer subtraction was performed using beamline specific software.[34]

SAXS Data Processing and Analysis. SAXS curves from different exposures and concentrations were scaled and merged using SCÅTTER. Anomalously large errors due to incomplete detector masking were manually adjusted using neighboring error measurements. Data were truncated to q = 0.26 $Å^{-1}$ based on nonideal buffer subtraction at q > 0.3 $Å^{-1}$ indicated by volume-of-correlation analysis.[35]

Interpretation of the SAXS Data Using Structural Models. The SAXS data were interpreted using multiple-atomic resolution structural models of wt-ERAP1 and 4mut-ERAP1 from the cMD calculations and the MultiFoXS methodology.[36] In brief, SAXS profiles (the scattering intensity of a molecule as a function of spatial frequency) were computed for the cMD conformations using FoXS[37] and then fitted to the

DOI: 10.1021/acs.biochem.6b01170
Biochemistry XXXX, XXX, XXX−XXX

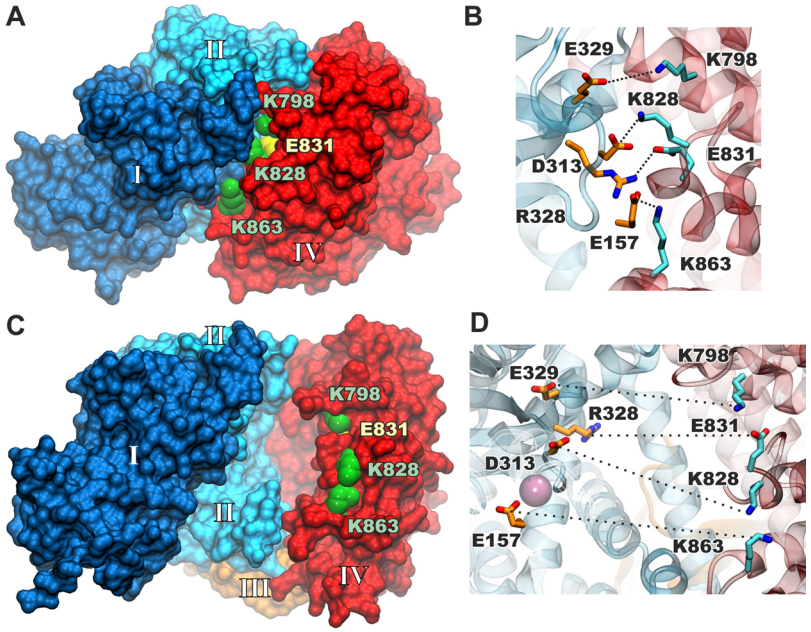

Figure 1. Schematic representations of ERAP1 in the (A and B) closed and (C and D) open states, illustrating the position of the four residues mutated to glutamine. ERAP1 domains are color-coded with blue, cyan, orange, and red for domains I–IV, respectively.

experimental SAXS profiles by optimizing a scale factor (c), the excluded volume (c_1), and the hydration layer density (c_2) parameters to minimize the χ score:

$$\chi = \sqrt{\frac{1}{S}\sum_{i=1}^{s}\left[\frac{I_{exp}(q_i) - c\sum_n w_n I_n(q_i, c_1, c_2)}{\sigma(q_i)}\right]^2}$$

where S is the number of points, $I_{exp}(q)$ is the experimental profile, $I_n(q,c_1,c_2)$ and w_n are the computed profile and the corresponding weight for each of the N conformational states, respectively, and $\sigma(q)$ is the experimental error of the profile. Enumeration of multistate models is performed iteratively using a branch-and-bound method, in which each step the K best-scoring models (typically, K = 10000) of size n (typically, $1 < n < 5$) are extended to KN models of size $n + 1$ by adding each of the N conformations given.[38] To minimize data overfitting in multistate models, the scoring function is employed with a single set of c_1 and c_2 values for all N states.

Input conformations for the FoXS server and MultiFoXS were extracted from the cMD trajectories of both open ERAP1 constructs after agglomerative clustering of 15000 snapshots, using a variable minimum distance between clusters (e). For e = 1.5 Å, the cMD trajectories resulted in 87 clusters of wt-ERAP1 and 92 clusters of 4mut-ERAP1. For e = 1.0 Å, wt-ERAP1 resulted in 1687 clusters and 4mut-ERAP1 in 1535 clusters. The all-atom representative members (centroids) of these 3222 clusters in addition to two representative members from the cMD trajectories of ERAP1 in the closed state and the four initial models were used after backbone RMSD fitting with respect to domain III (residues 530–614).

RESULTS

Design of ERAP1 Variants with Perturbed Interdomain Interactions. To examine how interdomain interactions affect ERAP1 conformation and function, we selected four residues in domain IV of ERAP1 that form salt-bridge electrostatic interactions in the closed conformation with residues in domains I and II of ERAP1, namely, K828, E831, K798, and K863. All residues were mutated to Q to abrogate the charge without altering the overall hydrophilicity of the side chain. Mutations were performed in sets of two, generating two ERAP1 variants, K828Q/E831Q (henceforth named 2mut-ERAP1) and K828Q/E831Q/K798Q/K863Q (henceforth named 4mut-ERAP1). These mutations are expected to abrogate specific electrostatic interactions in the closed conformation of ERAP1 and have a weaker effect in the open conformation in which they are distal from their interacting partners in domains I and II (Figure 1). It should be noted, however, that electrostatic interactions can exert some effect at a distance, and as a result, these mutations may have some influence on open conformations, albeit to a smaller degree than in the closed conformation.

Enzymatic Analysis of ERAP1 Variants. To evaluate effects of the mutations on enzymatic activity, we measured the specific activity of the ERAP1 variants on the hydrolysis of the well-established model substrate L-AMC. Both variants were found to be one order of magnitude less active in hydrolyzing this substrate, suggesting that the mutations, although distal from the enzyme's active site, can negatively impact the catalytic potency of the enzyme (Figure 2). This effect was not limited to small substrates because the hydrolysis of the 10mer peptidic fluorigenic substrate WRVYEC(dnp)ALK[16] was also catalyzed more slowly by the variants (3-fold slower for 2mut-ERAP1 and 4-fold slower for 4mut-ERAP1) (Figure S1).

To investigate this further, we performed Michaelis–Menten (MM) analysis of the wild-type protein and the two variants. For this analysis, we utilized the chromogenic substrate L-pNA because L-AMC has a very large K_M value, making MM analysis difficult since inner filter effects from the substrate complicate fluorescence measurements.[13] As for the L-AMC substrate, we found that the catalytic rate was much lower for the variants at low substrate concentrations. Surprisingly, however, MM analysis of the variants fit an allosteric model with kinetic parameters (K_{prime}, V_{max}, and Hill value) being much higher for the variants (Figure 2B). In particular, the Hill value for the

DOI: 10.1021/acs.biochem.6b01170
Biochemistry XXXX, XXX, XXX–XXX

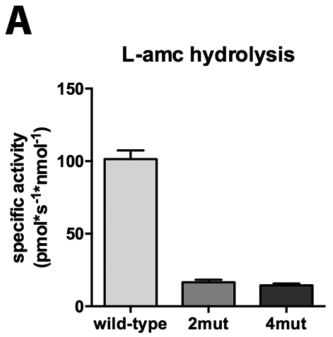

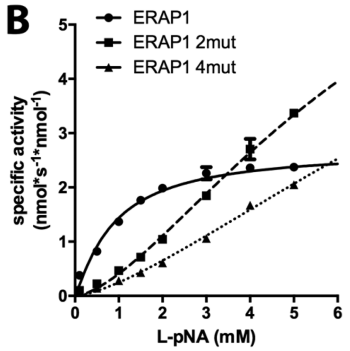

	wild-type	2mut	4mut
K_{prime} (mM)	0.88±0.13	21±3	39±16
V_{max} (nmol*s^{-1} *nmol^{-1})	2.7±0.2	9±2	10±4
Hill value	1.1±0.1	1.6±0.1	1.4±0.1

Figure 2. (A) Specific activity of hydrolysis of the model fluorigenic substrate L-AMC by ERAP1 and ERAP1 variants. (B) Michaelis–Menten analysis of ERAP1 and ERAP1 variants using as a substrate the chromogenic compound L-pNA. Lines represent nonlinear regression fits to either classical or allosteric MM kinetics. Error bars represent the standard deviation of triplicate experiments (only shown when sufficiently large to be visible on the graph).

wild type was close to one (1.1 ± 0.1), indicating either no or very limited cooperativity, but it increased to 1.6 ± 0.1 and 1.4 ± 0.1 for 2mut- and 4mut-ERAP1, respectively (Figure 2B). To confirm the classical-to-allosteric shift in kinetic behavior, we employed the corrected Akaike's Information Criterion test (AICc). The AICc values for wild-type ERAP1 were −72 and −74 for the allosteric and classical models, respectively, indicating that the classical model is probably more appropriate (2.9 times more likely to be correct). For 2mut-ERAP1, the same analysis resulted in AICc values of −82 and −58, respectively, indicating that the allosteric model is >10^5 times more likely to be correct. Similarly for 4mut-ERAP1, the AICc values were −96 and −69 for the allosteric and classical models, respectively, indicating that the allosteric model is >10^6 times more likely to be correct. This change in kinetic behavior resulted in the variants having lower activity at low substrate concentrations, but this was reversed at high concentrations, indicating a possible bottleneck in the activity of the wild-type enzyme that is not shared in the mutants. One possible explanation is that the maximal rate of turnover for the wild-type enzyme is limited by the opening of the fully closed conformation, a transition that is facilitated in the variants.

It has been previously shown that small substrate hydrolysis by ERAP1 can be activated by peptides, and this has been suggested to be a key component of the length selectivity mechanism through a process of self-activation by longer peptides.[13] Given the changes in MM parameters in the mutants and the strong shift to allosteric kinetics, we investigated whether the mutations also affected this property of ERAP1. Three model peptide substrates were tested, including a nonhydrolyzable peptide analogue (Figure 3A). In

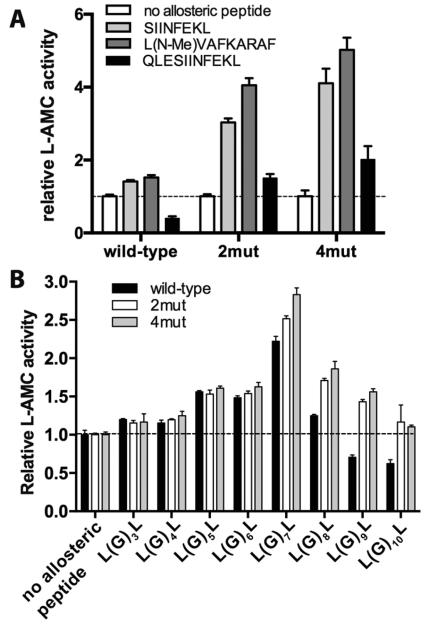

Figure 3. (A) Specific activity of ERAP1 and variants for the hydrolysis of fluorigenic substrate L-AMC in the presence or absence of peptides SIINFEKL, L(N-Me)VAFKARAF, and QLESIINFEKL. (B) Relative enzymatic activity in the presence of LG_nL peptides, where n = 3–10. The dotted line indicates activity normalized in the absence of peptide.

all cases, the variants were activated to a much higher degree than the wild-type enzyme, with 4mut exhibiting an activation that was stronger than that of 2mut. Surprisingly, the longer peptide QLESIINFEKL was found to inhibit wild-type ERAP1 but activate both variants. This enhanced activation could partially restore the reduced activity of the variants (Figure S2), indicating that the mutations affect the mechanism of ERAP1 without directly compromising its catalytic efficacy. It is conceivable that by disrupting electrostatic domain interactions we inadvertently generated ERAP1 variants in which peptide binding makes a greater contribution to the energetics of the conformational change.

ERAP1 has been reported to show preferences for more than eight residues, consistent with its biological function in trimming longer antigenic peptide precursors.[13,15] To investigate if the mutations affected the ability of ERAP1 to select for longer peptides, we measured the rate of trimming of the N-terminal leucine residue from a series of LG_nL peptides, where n = 3–10. It has been previously demonstrated that ERAP1 will trim the largest peptides from this series much faster than the smaller ones.[13,15] Although the mutations had effects on the overall trimming rates of these peptides similar to the effects for small substrates, they did not affect the overall length selection (Figure S3). These results suggest that the strength of interaction between domains II and IV is not critical to the ability of ERAP1 to select for peptide length.

DOI: 10.1021/acs.biochem.6b01170
Biochemistry XXXX, XXX, XXX–XXX

ERAP1 can also be activated by some of the LG_nL peptides[13] in a length-dependent manner. This activation is indistinguishable between the wild-type and variant enzymes for peptides up to eight amino acids in length (Figure 3B). Strikingly, however, the variants were activated to a higher degree by peptides of more than nine amino acids, and this difference resulted in 11mer peptides activating the variants but inhibiting the wild type (this result is consistent with the QLESIINFEKL peptide described above). This result suggests differences in peptide recognition between wild-type ERAP1 and the variants possibly related to a more open conformation for the variants that can interact with and be activated by longer peptides.

Comparison of the crystal structures of the two conformations of ERAP1 has suggested that the active site is reorganized between the open and closed conformations. Specifically, the catalytic Tyr438 is reoriented toward the Zn(II) atom in the closed state, and Phe433, a key residue for the formation of the S1 specificity pocket, is disordered in the open state.[12] These differences may affect binding of the inhibitor to the active site.[39] We utilized the competitive mechanism-based inhibitor, DG013A, to probe the integrity of the active site of ERAP1 and how it is affected by the interdomain interactions.[40] The inhibitor was found to bind strongly to wild-type ERAP1 (IC_{50} = 36 nM) but with reduced affinity for the 2mut variant (IC_{50} = 225 nM) and further reduced affinity for the 4mut variant (IC_{50} = 836 nM), indicating that mutations that interfere with domain interactions away from the catalytic site can affect the affinity of a competitive inhibitor (Figure 4A). To further investigate this effect, we analyzed the kinetics of binding and release of DG013A on wild-type ERAP1 and its variants (Figures S4 and S5). Because of the lower affinity of DG013A for 4mut, it was not possible to accurately measure binding kinetics, so we limited the comparison between wild-type ERAP1 and 2mut-ERAP1. The association kinetics for DG013A were similar between wild-type ERAP1 and 2mut (Figure 4B). The dissociation rate, however, was almost 20-fold faster for 2mut-ERAP1, a measurement that can account for the reduced IC_{50} for this variant. We conclude that perturbations on the interdomain interactions can affect the organization of the ERAP1 active site, leading to less kinetically stable inhibitor−enzyme complexes. One possible model that could explain this result is that the inhibitor on rates are primarily determined by initial capture by the open ERAP1 conformation and that the apparent off rates are determined by both the conformational change from closed to open, a conformational change necessary to provide access to the solvent, and inhibitor dissociation. Disruption of interdomain interactions that stabilize the closed ERAP1 can produce faster off rates by facilitating the transition to the open state.

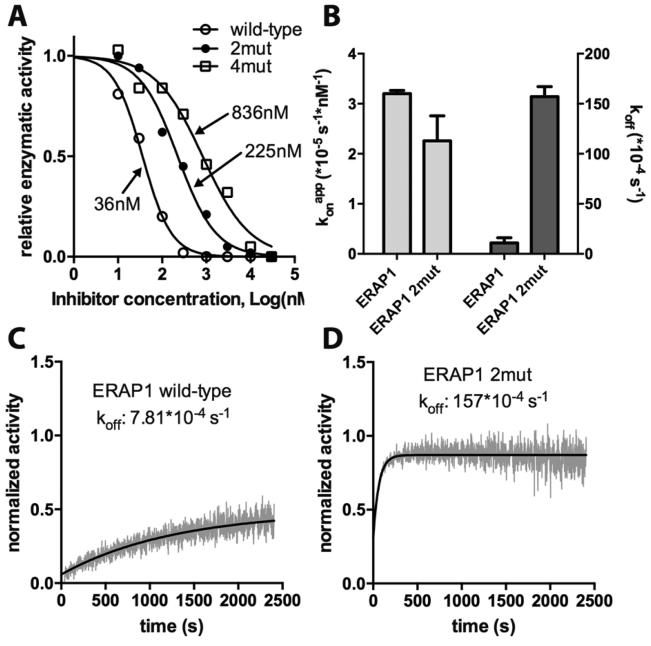

Figure 4. (A) Titration curves of inhibitor DG013A with wt-ERAP1 and its variants. Calculated IC_{50} values are indicated for each trace. (B) Calculated k_{on} and k_{off} parameters for the interaction of DG013A with ERAP1 and ERAP1 variant 2mut. (C) Representative kinetic trace of recovery of ERAP1 activity after dilution of an ERAP1/DG013A mixture. Data were fit to an exponential association equation. (D) Same as panel C, but using 2mut-ERAP1.

Conformational Dynamics of ERAP1 Sampled by cMD and aMD Simulations. In an effort to put these functional findings in a structural perspective, we analyzed the effect of the mutations on the conformational dynamics of ERAP1 using molecular dynamics. To simulate the enzyme as closely as possible to the experimental conditions, we prepared a model of ligand-free ERAP1 that was more complete than the one previously described,[15] by modeling a 13-residue N-terminus, a C-terminal six-His tag, and four N-linked glycan moieties resolved in the crystallographic structures (Figures S6 and S7), and used this model for cMD and aMD calculations. It should be noted that the experimental construct of ERAP1 used in this study is based on the sequence of ancestral ERAP1 isoform 1 (Figure S6), with the inclusion of the R127P polymorphism. The initial models of wild-type ERAP1 and 4mut constructs (Figure 1) were prepared as described in detail in Computational Methods. Preparation of the Simulation Systems, and 0.5 μs cMD simulations were performed for each of the three initial conformations of open ERAP1, in addition to a 0.5 μs cMD simulation of ERAP1 in the closed state (Table S1). The simulations of both ERAP1 constructs that were initiated at the closed state remained closed, in contrast to the simulations initiated from open states that displayed large conformational variability.

To obtain the collective motions of ERAP1 in the open states, cMD trajectories were analyzed by means of principal component analysis (PCA), which revealed two major modes: a motion describing the open-to-closed transition [PC-1 (Figure 5A)] and a twist motion between N- and C-terminal domains I and IV [PC-2 (Figure 5B)]. To help with the analysis of the MD results, we defined two variables: an interdomain angle θ, defined as the angle among lines connecting the centers of mass of domains I and II, III, and IV, and interdomain torsion angle φ, defined as the angle between two planes that traverse domains I and II and domain IV (Figure 5C,D). To further explore the conformational sampling by ERAP1, we employed aMD simulations that were seeded from the cMD trajectories at different states of conformational subspace. Ten independent aMD calculations of 50 million 2 fs steps were performed for each construct, which were initiated at θ values ranging from 60° to 72° (Figures S12 and S13).

Examination of the distributions of interdomain angle θ from the cMD simulations of both ERAP1 constructs in the open states (Figure S10) reveals that wt-ERAP1 sampled a range of 58−75° with maxima at 62° and 68°, while 4mut-ERAP1 sampled a similar range of 59−72° with maxima at 63° and 67°

DOI: 10.1021/acs.biochem.6b01170
Biochemistry XXXX, XXX, XXX−XXX

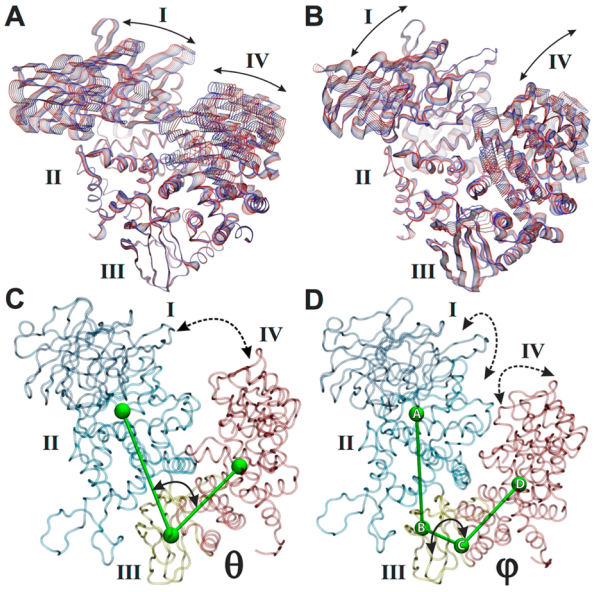

Figure 5. (A and B) Representative structures illustrating the motions of ERAP1 along the two principal components extracted from cMD simulations of wt-ERAP1 in the open state. The color scale is from red (open) to blue (closed). (C and D) Definition of collective variables θ and φ, the interdomain angle and torsion, respectively, which were used to describe the basic motions of the transition of ERAP1 between open and closed states. Roman numerals indicate the four domains. φ is defined as the angle between the A−B−C and B−C−D planes as indicated in panel D.

(Figure S11). Projection of the cMD trajectories on the subspace of the two collective variables, θ and φ, reveals two qualitatively similar free energy profiles for wt-ERAP1 and 4mut-ERAP1 (Figure 6A). The simulations of both constructs visit several semiclosed substrates but cannot reach fully closed conformations on the microsecond time scale (for comparison, the projections of the cMD simulations of ERAP1 in the closed states are shown in the inset of Figure 6A). Although the relative populations favor a more closed wt-ERAP1 with respect to 4mut-ERAP1, differences between them are not significant and most probably hampered by low statistical mechanical sampling.

Investigation of the distributions of θ from the aMD trajectories revealed that wt-ERAP1 converged to a conformational subspace of partially closed states centered at θ = 57°, whereas 4mut-ERAP1 sampled more semiclosed states around θ = 61° (Figure S14). Boltzmann-reweighted projection of the aMD trajectories onto the θ/φ subspace revealed that aMD simulations covered a larger amount of phase space between the open and closed states of ERAP1 (Figure 6B). The free energy profile of wt-ERAP1 is highly structured and rugged, exhibiting a broad distribution of populations in the subspace sampled between open and closed states. In contrast, the simulations of 4mut-ERAP1 display a well-defined energy basin at semiclosed conformations of θ = 60−62°, indicating higher energy barriers to reach the fully closed state. Although aMD simulations cannot reproduce the exact dynamics of the system and accurate population analysis of such a complex phase space is very demanding, our simulations suggest that the open−closed transition in wt-ERAP1 can be accessed on the millisecond time scale and relatively low energy barriers (<10

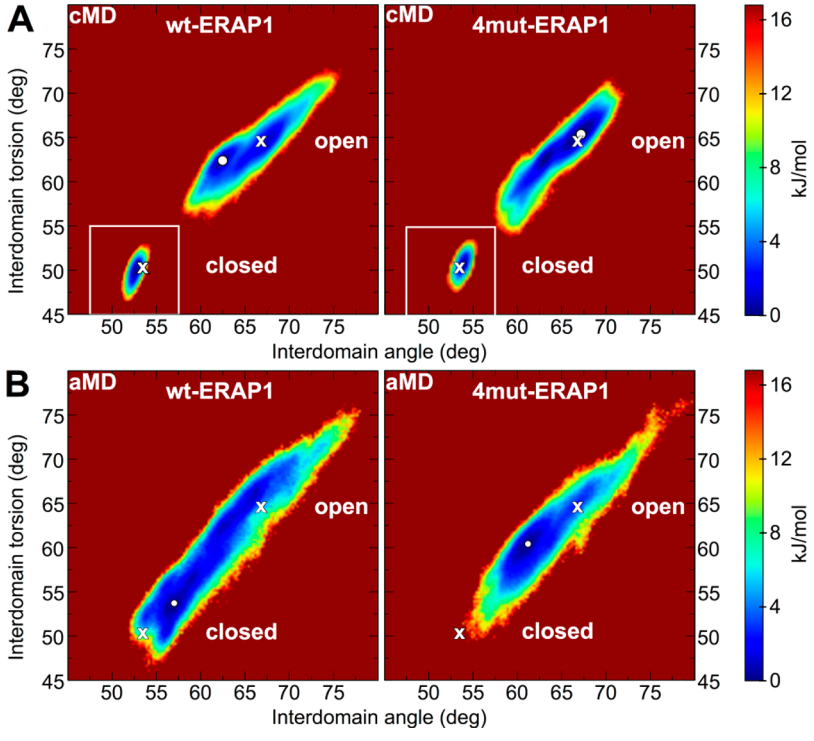

Figure 6. Free energy profiles of wt-ERAP1 and 4mut-ERAP1 sampled by (A) cMD and (B) aMD simulations in the open state. Insets are the corresponding plots from the cMD simulations of ERAP1 in the closed state. Graphs were generated by Boltzmann-weighted projection of the cMD and aMD trajectories on the two collective variables, interdomain angle θ and interdomain torsion φ (Figure 2). aMD trajectories were reweighted on the basis of a Maclaurin series expansion to the 10th order. The projections of the crystallographically based models are indicated with crosses, and white circles indicate free energy minima.

DOI: 10.1021/acs.biochem.6b01170
Biochemistry XXXX, XXX, XXX−XXX

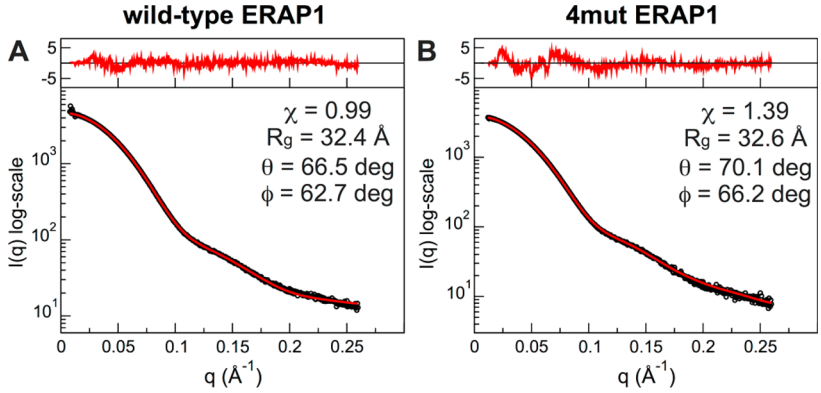

Figure 7. Comparison of the experimental SAXS profiles (●) with the best-fitting computed SAXS profiles (red line) of wt-ERAP1 and 4mut-ERAP1 models. The top plots display the residuals corresponding to the difference between the experimental and computed intensities weighted by the experimental uncertainty, $[I_{exp}(q) - I_{calc}(q)]/\sigma_{exp}(q)$.

kJ/mol), whereas 4mut-ERAP1 preferentially populates a semiclosed conformation with higher energy barriers (>16 kJ/mol) toward the fully closed state.

SAXS Analysis of ERAP1 Variants in Solution. To investigate the conformational state of ERAP1 in solution as well as the effect of the mutations, we analyzed wt-ERAP1 and 4mut-ERAP1 by small-angle X-ray scattering (SAXS). Model-independent analysis using AUTORG indicated that the hydrodynamic radius (R_H) in solution is 33.43 ± 0.35 Å for wt-ERAP1 and 33.84 ± 0.45 Å for 4mut-ERAP1. These diameters are consistent with a predominately open conformation for both the wild type and the ERAP1 variant and suggest that the overall average structure of ERAP1 is not affected by the mutations. Indeed, although MD simulations predict structural alterations due to the mutations, these are interdomain motions that result in very small effects in overall protein shape (Figures 5 and 6) that may not be readily apparent by model-independent SAXS analysis.

In an effort to gain further structural insight using the SAXS data, we attempted to generate an atomic model that fits the experimental SAXS profiles using the open-source FoXS methodology.[37] An attempt to fit the crystallographic structures of ERAP1 in the open and closed states (PDB entries 3MDJ and 2YD0, respectively) at the experimental SAXS profiles resulted in a χ of >4.4 for the open states and a χ of >20 for closed ERAP1 (Figure S15A,B), indicating that the open state better describes the structure of the ERAP1 constructs in solution. Considering, however, that X-ray structures with missing hydrogen atoms and protein regions are not optimal models for fitting the SAXS data, we used the all-atom initial models employed in the MD simulations. The fit of the experimental data improved to χ values of 2.9 and 2.8 for wt-ERAP1 and 4mut-ERAP1, respectively, using the chain C model of PDB entry 3MDJ (Figure S15C,D). Again, the closed conformation of the wt-ERAP1 model displayed a poor fit (χ > 13).

Considering the wide distribution of open ERAP1 states observed in our MD simulations, we hypothesized that an ensemble of representative conformations from the 500 ns cMD trajectories of both constructs might be a more powerful approach for identifying conformations to explain SAXS data than simple fitting of a single X-ray structure. Clustering of 15000 snapshots from the cMD trajectories of each construct in the open state with a minimal distance between clusters of 1.0 Å resulted in 1687 and 1536 clusters for wt-ERAP1 and 4mut-ERAP1, respectively, which were used as input models for the MultiFoXS program with a q_{max} of 0.26 Å^{-1}. The wt-ERAP1 models exhibited an excellent fit to the experimental SAXS profile with the best model displaying a χ of 0.99 (Figure 7) and the top 100 models in the χ range of 1.0−2.1 (Table S2). The best two-state model of wt-ERAP1 did not significantly improve the fit but did narrow the range of χ values of the top 100 two-state ensembles (χ = 1.0−1.3). 4mut-ERAP1 displayed remarkably good fits, too, with the best model at χ = 1.39 (Figure 7) and the top 100 models in the χ range of 1.4−2.1 (Table S2). The multistate modeling of 4mut-ERAP1 data improved the fit to the experimental SAXS profile to χ = 1.23 for two-state ensembles and χ = 1.19 for three-state ensembles (Table S2). The SAXS profile of wt-ERAP1 fits best to a θ = 66.5° and φ = 62.7° model. The SAXS profile of 4mut-ERAP1 fits to a θ = 70.1° and φ = 66.2° model, with the fit improved slightly for a two-state model with weighted θ = 68.9° and φ = 66.3° (Table S2). This could suggest that the open form of 4mut-ERAP1 might be somewhat less conformationally constrained than wt-ERAP1. However, the calculated radii of gyration (R_g) for the two best-fit structures are very similar, 32.4 Å for wt-ERAP1 and 32.6 Å for 4mut ERAP1, which, in conjunction with the similar model-independent hydrodynamic radii, suggest that the overall shape and size of the two proteins are similar in solution. Thus, SAXS analysis indicates that both wt-ERAP1 and 4mut-ERAP1 adopt a predominantly open conformational state in solution. The mutations do not have a major disruptive influence on the gross solution structure of ERAP1 but may have a weak effect on the exact orientation of domain IV in relation to domain II, or on the conformational dynamics of the protein, including the accessibility to closed conformations.

■ DISCUSSION

On the basis of the known crystal structures of ERAP1, we initially hypothesized that the open and closed conformations coexist in equilibrium in solution by performing discrete tasks for the catalytic cycle, namely substrate capture (open state) and reaction catalysis (closed state). According to this hypothesis, we analyzed the effect of ERAP1 variants that lack salt-bridge interactions that stabilize the juxtapositioning of domains I and II with domain IV in the closed structure. SAXS analysis of both wild-type and variant ERAP1, however, suggests that ERAP1 is on average in the open state in solution, a conformational state in which the mutated residues

DOI: 10.1021/acs.biochem.6b01170
Biochemistry XXXX, XXX, XXX−XXX

are apart from each other. Still, enzymatic analysis indicated major effects of the mutation on catalytic efficiency and mechanism. These can be rationalized by considering that electrostatic interactions can act at long range, albeit with reduced potency. Thus, the effects of the mutations on ERAP1 activity may be due to the disruption of long-range attractive electrostatic forces that would normally "guide" domain closing. An alternative but complementary interpretation is that the mutations destabilize the closed conformation. This possibility is supported by our aMD calculations that suggest that the 4mut-ERAP1 variant populates fewer closed states than wt-ERAP1 does.

Our analysis provides insight into the conformational dynamics of ERAP1. Although SAXS analysis suggests that on average ERAP1 is in an open conformation in solution, MD calculations suggest an energetically accessible continuous ensemble of conformations ranging from the open state to the closed state (although local minima are also evident). The latter suggests low energy barriers between the two states, as would be expected given that the conformational rearrangement during the ERAP1 catalytic cycle requires no continuous energy input (such as ATP hydrolysis). Furthermore, aMD calculations suggest that the ERAP1 conformational alteration occurs on the millisecond time scale, and the linearity of the relationship between the observed k_{on} and the inhibitor concentration (Figure S4B) suggests a lack of any kinetic bottleneck (such as a conformational change) during the time scale of the stopped-flow experiments, limiting the time scale of any conformational change in the subsecond region.

The biological role of ERAP1 in trimming N-terminally extended peptide precursors to the optimal length for binding to MHC class I molecules has been linked to some unique properties of this enzyme, namely, length and sequence selection.[13,41] Indeed, even when compared to ERAP2 and IRAP, the other two enzymes within the oxytocinase subfamily of M1 aminopeptidases, ERAP1 appears to be the most optimized for the specific role of trimming long peptides. Specifically, although ERAP1 is much slower in trimming small model substrates[42] than ERAP2 and IRAP are, it is very efficient in trimming large peptidic substrates. Accordingly, ERAP1 can be activated by small peptides, whereas ERAP2 and IRAP cannot.[43,44] This evidence suggests that despite their high degree of homology, ERAP2 and IRAP have key mechanistic differences from ERAP1, and the latter is the most specialized for trimming long antigenic peptide precursors. This is highlighted by a multitude of biological studies indicating ERAP1 as being the most important of the three in generating antigenic peptides and the most closely associated with disease predisposition in humans.

The mechanism behind the specialization of ERAP1 for large peptides has been suggested to include a conformational reorganization of the active site that includes reorientation of the catalytic Tyr438 and spatial optimization of residues that line the S1 selectivity pocket, activated by occupancy of a regulatory site by a C-terminal moiety of the peptide.[13,14] On the basis of crystallographic analysis of the two ERAP1 conformations, it has been hypothesized that interconversion between open and closed conformations underlies changes in catalytic efficacy, with the open structure being catalytically inefficient (or even inactive) and the closed conformation catalytically optimized. SAXS analysis presented here suggests that ERAP1 is predominantly in the open conformation in solution. This finding is consistent with the low catalytic turnover for small substrates that cannot promote the conformational change. In contrast, larger peptides can promote closing and result in higher rates of catalytic turnover. Disruption of key interdomain interactions in the two variants described here (2mut and 4mut) possibly destabilizes the closed conformation and alters the conformational landscape for ERAP1. This leads to an even lower rate of catalytic turnover in solution but also allows for a stronger activation by peptides: as the interactions between the domains are weakened, bridging interactions by the peptide can become more important for promoting the conformational change. Taken together, these insights can be used to propose an evolutionary model for peptide trimming by ERAP1 compared to other aminopeptidases: mutational disruption of optimized interdomain interactions in ERAP1 led to more open conformations in solution that although result in lower catalytic efficiency, make the enzyme specialized for larger peptides. This model would suggest that ERAP2 and possibly IRAP are in less open conformations in solution and therefore more catalytically efficient but less specialized for producing antigenic peptides (or rather are specialized for processing smaller peptides), although further structural studies of ERAP2 and IRAP are needed to confirm or disprove this hypothesis. This framework can also be used to explain the effects of disease-associated SNPs on the ERAP1 mechanism. SNPs away from the active site operate to affect the conformational dynamics of the enzyme and therefore affect the catalytic efficiency and peptide specialization indirectly, allowing for small adjustments in enzymatic activities that underpin changes in the immunopeptidome and immune system variability among individuals.[9,15]

Despite the importance of ERAP1 in regulating adaptive immune responses, the literature contains very few examples of potent competitive ERAP1 inhibitors that are also selective for other aminopeptidases and in particular for ERAP2 and IRAP. The findings presented here regarding the conformation of ERAP1 in solution provide a basis for understanding any difficulty in rationally designing ERAP1 inhibitors. If ERAP1 is primarily in the open conformation in solution, designing ERAP1 inhibitors based on the closed conformation[40,45] may not be the optimal approach. Accordingly, inhibitors optimized for the closed conformation would be expected to have trouble forming good initial encounter complexes with the open conformation of ERAP1, resulting in reduced apparent affinity. On the other hand, the poorly organized S1 pocket of ERAP1 in the open conformation presents significant challenges in inhibitor design but may be the appropriate species to target for achieving selectivity. An alternative approach may be to select for allosteric ERAP1 inhibitors that "lock" the open state or preclude the formation of the closed state.

ERAP1 has been reported to also trim N-extended peptides while the peptides are bound to MHC,[46,47] although another study found that the MHC rather protected the peptide from ERAP1 trimming.[48] Previous modeling work suggested that an MHC-bound peptide would have to protrude at least six to seven residues from the MHCI to reach the active site of ERAP1 in the open conformation, unless large-scale conformational changes not so far observed in MHCI can occur.[13] Molecular dynamics calculations have suggested that slightly more open conformations are structurally feasible for ERAP1,[15] and it is possible that weakening interdomain interactions may allow for easier access to such more open conformations, potentially enhancing the ability of ERAP1 to trim peptides that

DOI: 10.1021/acs.biochem.6b01170
Biochemistry XXXX, XXX, XXX−XXX

are bound to MHCI. Further enzymatic and structural work is needed to clarify the relative efficiency and mechanisms of this process.

In summary, we have used structure-guided site-directed mutagenesis in combination with computational modeling and small-angle X-ray scattering to probe the importance of interdomain electrostatic interaction on the catalytic mechanism and efficiency of ERAP1. Our findings suggest that such interactions are central to the mechanism of the enzyme and probably underlie its specialization for large peptides. The conformational plasticity of ERAP1 presents a hurdle in inhibitor development and needs to be taken into account or even exploited for developing selective inhibitors for this enzyme.

■ ASSOCIATED CONTENT

Supporting Information

The Supporting Information is available free of charge on the ACS Publications website at DOI: 10.1021/acs.biochem.6b01170.

A table listing the simulation systems employed for molecular dynamics calculations, a table listing the MultiFoXS results for the two ERAP1 constructs, rates of hydrolysis of the fluorigenic peptide by wt-ERAP1 and its variants, rates of hydrolysis of the L-AMC substrate by ERAP1 and its variants in the absence or presence of peptide QLESIINFEKL, specific activity of ERAP1 and its variants for the hydrolysis of the N-terminus of LG_nL peptides, representative kinetic traces from stopped-flow experiments, a graph showing the linear relationship of the DG013A association rate to the inhibitor concentration, first-order derivative traces of the kinetics of DG013A association with ERAP1 and ERAP1 mut2, sequence of human ERAP1 used for computational studies, graphical representation of the wild-type ERAP1 model used in computational studies, animations illustrating the protein motions based on MD simulations, plots of the interdomain angle as a function of simulation time, plots showing the distribution of interdomain angles and dihedral angles from MD simulations, and FoXS analysis results (PDF)

■ AUTHOR INFORMATION

Corresponding Author

*National Centre for Scientific Research Demokritos, Agia Paraskevi, 15341 Athens, Greece. E-mail: stratikos@rrp.demokritos.gr or stratikos@gmail.com. Telephone: +30-210-6503918. Fax: +30-210-6543526.

ORCID

Athanasios Papakyriakou: 0000-0003-3931-6232

Efstratios Stratikos: 0000-0002-3566-2309

Author Contributions

A.S. performed site-directed mutagenesis and purified recombinant proteins with help from A.M. A.S. performed the enzymatic analysis and interpreted data. Z.M. purified recombinant proteins, performed the SAXS analysis, and interpreted data. A.P. performed the computational modeling and analyzed and interpreted data. P.K. and D.G. provided the DG013A inhibitor. L.J.S. supervised the structural analysis, analyzed and interpreted data, and supervised the project with E.S. E.S. conceived and supervised the project, analyzed and interpreted data, and wrote the paper with help from all authors.

Funding

This research was financed by the European Union (European Social Fund) and Greek national funds through the Operational Program "Education and Lifelong Learning" of the National Strategic Reference Framework: Research Funding Program of the General Secretariat for Research & Technology (Grant ERC-14 to E.S.), and from the National Institutes of Health (Grant AI038996 to L.J.S.). Funding was also provided by the Harry J. Lloyd Charitable Trust (to E.S.). The use of infrastructure associated with the National Research Infrastructure in Structural Biology, INSTRUCT-EL for recombinant protein production, and computational analysis is also acknowledged. X-ray scattering analysis was conducted at the Advanced Light Source (ALS), a national user facility operated by Lawrence Berkeley National Laboratory on behalf of the U.S. Department of Energy (DOE), Office of Basic Energy Sciences, through the Integrated Diffraction Analysis Technologies (IDAT) program, supported by the DOE Office of Biological and Environmental Research. Additional support comes from the National Institutes of Health project MINOS for experimentation at the SIBYLS beamline (Grant GM105404).

Notes

The authors declare no competing financial interest.

■ ABBREVIATIONS

ERAP1, endoplasmic reticulum aminopeptidase 1; PCA, principle component analysis; SAXS, small-angle X-ray scattering; cMDs, classical molecular dynamics; aMDs, accelerated molecular dynamics.

■ REFERENCES

(1) Evnouchidou, I., Papakyriakou, A., and Stratikos, E. (2009) A New Role for Zn(II) Aminopeptidases: Antigenic Peptide Generation and Destruction. *Curr. Pharm. Des. 15*, 3656−3670.

(2) Weimershaus, M., Evnouchidou, I., Saveanu, L., and van Endert, P. (2013) Peptidases Trimming MHC Class I Ligands. *Curr. Opin. Immunol. 25*, 90−96.

(3) Aldhamen, Y. A., Pepelyayeva, Y., Rastall, D. P., Seregin, S. S., Zervoudi, E., Koumantou, D., Aylsworth, C. F., Quiroga, D., Godbehere, S., Georgiadis, D., Stratikos, E., and Amalfitano, A. (2015) Autoimmune Disease-Associated Variants of Extracellular Endoplasmic Reticulum Aminopeptidase 1 Induce Altered Innate Immune Responses by Human Immune Cells. *J. Innate Immun. 7*, 275−289.

(4) Hisatsune, C., Ebisui, E., Usui, M., Ogawa, N., Suzuki, A., Mataga, N., Takahashi-Iwanaga, H., and Mikoshiba, K. (2015) Erp44 Exerts Redox-Dependent Control of Blood Pressure at the ER. *Mol. Cell 58*, 1015−1027.

(5) Stratikos, E. (2014) Modulating Antigen Processing for Cancer Immunotherapy. *Oncoimmunology 3*, e27568.

(6) Chen, L., Ridley, A., Hammitzsch, A., Al-Mossawi, M. H., Bunting, H., Georgiadis, D., Chan, A., Kollnberger, S., and Bowness, P. (2016) Silencing or Inhibition of Endoplasmic Reticulum Aminopeptidase 1 (ERAP1) Suppresses Free Heavy Chain Expression and Th17 Responses in Ankylosing Spondylitis. *Ann. Rheum. Dis. 75*, 916−923.

(7) Evnouchidou, I., Birtley, J., Seregin, S., Papakyriakou, A., Zervoudi, E., Samiotaki, M., Panayotou, G., Giastas, P., Petrakis, O., Georgiadis, D., Amalfitano, A., Saridakis, E., Mavridis, I. M., and Stratikos, E. (2012) A Common Single Nucleotide Polymorphism in Endoplasmic Reticulum Aminopeptidase 2 Induces a Specificity

DOI: 10.1021/acs.biochem.6b01170
Biochemistry XXXX, XXX, XXX−XXX

Switch That Leads to Altered Antigen Processing. *J. Immunol. 189*, 2383−2392.
(8) Saveanu, L., Carroll, O., Weimershaus, M., Guermonprez, P., Firat, E., Lindo, V., Greer, F., Davoust, J., Kratzer, R., Keller, S. R., Niedermann, G., and van Endert, P. (2009) IRAP Identifies an Endosomal Compartment Required for MHC Class I Cross-Presentation. *Science 325*, 213−217.
(9) Reeves, E., Colebatch-Bourn, A., Elliott, T., Edwards, C. J., and James, E. (2014) Functionally Distinct Erap1 Allotype Combinations Distinguish Individuals with Ankylosing Spondylitis. *Proc. Natl. Acad. Sci. U. S. A. 111*, 17594−17599.
(10) Evnouchidou, I., Kamal, R. P., Seregin, S. S., Goto, Y., Tsujimoto, M., Hattori, A., Voulgari, P. V., Drosos, A. A., Amalfitano, A., York, I. A., and Stratikos, E. (2011) Coding Single Nucleotide Polymorphisms of Endoplasmic Reticulum Aminopeptidase 1 Can Affect Antigenic Peptide Generation in Vitro by Influencing Basic Enzymatic Properties of the Enzyme. *J. Immunol. 186*, 1909−1913.
(11) Haroon, N., and Inman, R. D. (2010) Endoplasmic Reticulum Aminopeptidases: Biology and Pathogenic Potential. *Nat. Rev. Rheumatol. 6*, 461−467.
(12) Stratikos, E., and Stern, L. J. (2013) Antigenic Peptide Trimming by Er Aminopeptidases–Insights from Structural Studies. *Mol. Immunol. 55*, 212−219.
(13) Nguyen, T. T., Chang, S. C., Evnouchidou, I., York, I. A., Zikos, C., Rock, K. L., Goldberg, A. L., Stratikos, E., and Stern, L. J. (2011) Structural Basis for Antigenic Peptide Precursor Processing by the Endoplasmic Reticulum Aminopeptidase Erap1. *Nat. Struct. Mol. Biol. 18*, 604−613.
(14) Kochan, G., Krojer, T., Harvey, D., Fischer, R., Chen, L., Vollmar, M., von Delft, F., Kavanagh, K. L., Brown, M. A., Bowness, P., Wordsworth, P., Kessler, B. M., and Oppermann, U. (2011) Crystal Structures of the Endoplasmic Reticulum Aminopeptidase-1 (ERAP1) Reveal the Molecular Basis for N-Terminal Peptide Trimming. *Proc. Natl. Acad. Sci. U. S. A. 108*, 7745−7750.
(15) Stamogiannos, A., Koumantou, D., Papakyriakou, A., and Stratikos, E. (2015) Effects of Polymorphic Variation on the Mechanism of Endoplasmic Reticulum Aminopeptidase 1. *Mol. Immunol. 67*, 426−435.
(16) Evnouchidou, I., Berardi, M. J., and Stratikos, E. (2009) A Continuous Fluorigenic Assay for the Measurement of the Activity of Endoplasmic Reticulum Aminopeptidase 1: Competition Kinetics as a Tool for Enzyme Specificity Investigation. *Anal. Biochem. 395*, 33−40.
(17) Fiser, A., and Sali, A. (2003) Modeller: Generation and Refinement of Homology-Based Protein Structure Models. *Methods Enzymol. 374*, 461−491.
(18) Anandakrishnan, R., Aguilar, B., and Onufriev, A. V. (2012) H++ 3.0: Automating Pk Prediction and the Preparation of Biomolecular Structures for Atomistic Molecular Modeling and Simulations. *Nucleic Acids Res. 40*, W537−541.
(19) Case, D. A., Cheatham, T. E., 3rd, Darden, T., Gohlke, H., Luo, R., Merz, K. M., Jr., Onufriev, A., Simmerling, C., Wang, B., and Woods, R. J. (2005) The Amber Biomolecular Simulation Programs. *J. Comput. Chem. 26*, 1668−1688.
(20) Maier, J. A., Martinez, C., Kasavajhala, K., Wickstrom, L., Hauser, K. E., and Simmerling, C. (2015) Ff14sb: Improving the Accuracy of Protein Side Chain and Backbone Parameters from Ff99sb. *J. Chem. Theory Comput. 11*, 3696−3713.
(21) Kirschner, K. N., Yongye, A. B., Tschampel, S. M., Gonzalez-Outeirino, J., Daniels, C. R., Foley, B. L., and Woods, R. J. (2008) Glycam06: A Generalizable Biomolecular Force Field. Carbohydrates. *J. Comput. Chem. 29*, 622−655.
(22) Papakyriakou, A., Spyroulias, G. A., Sturrock, E. D., Manessi-Zoupa, E., and Cordopatis, P. (2007) Simulated Interactions between Angiotensin-Converting Enzyme and Substrate Gonadotropin-Releasing Hormone: Novel Insights into Domain Selectivity. *Biochemistry 46*, 8753−8765.
(23) Jorgensen, W. L., Chandrasekhar, J., Madura, J. D., Impey, R. W., and Klein, M. L. (1983) Comparison of Simple Potential Functions for Simulating Liquid Water. *J. Chem. Phys. 79*, 926−935.
(24) Salomon-Ferrer, R., Gotz, A. W., Poole, D., Le Grand, S., and Walker, R. C. (2013) Routine Microsecond Molecular Dynamics Simulations with Amber on Gpus. 2. Explicit Solvent Particle Mesh Ewald. *J. Chem. Theory Comput. 9*, 3878−3888.
(25) Ryckaert, J. P., Ciccotti, G., and Berendsen, H. J. C. (1977) Numerical-Integration of Cartesian Equations of Motion of a System with Constraints - Molecular-Dynamics of N-Alkanes. *J. Comput. Phys. 23*, 327−341.
(26) Pastor, R. W., Brooks, B. R., and Szabo, A. (1988) An Analysis of the Accuracy of Langevin and Molecular-Dynamics Algorithms. *Mol. Phys. 65*, 1409−1419.
(27) Berendsen, H. J. C., Postma, J. P. M., Vangunsteren, W. F., Dinola, A., and Haak, J. R. (1984) Molecular-Dynamics with Coupling to an External Bath. *J. Chem. Phys. 81*, 3684−3690.
(28) Darden, T., York, D., and Pedersen, L. (1993) Particle Mesh Ewald - an N.Log(N) Method for Ewald Sums in Large Systems. *J. Chem. Phys. 98*, 10089−10092.
(29) Hamelberg, D., Mongan, J., and McCammon, J. A. (2004) Accelerated Molecular Dynamics: A Promising and Efficient Simulation Method for Biomolecules. *J. Chem. Phys. 120*, 11919−11929.
(30) Hamelberg, D., de Oliveira, C. A. F., and McCammon, J. A. (2007) Sampling of Slow Diffusive Conformational Transitions with Accelerated Molecular Dynamics. *J. Chem. Phys. 127*, 155102.
(31) Miao, Y. L., Sinko, W., Pierce, L., Bucher, D., Walker, R. C., and McCammon, J. A. (2014) Improved Reweighting of Accelerated Molecular Dynamics Simulations for Free Energy Calculation. *J. Chem. Theory Comput. 10*, 2677−2689.
(32) Roe, D. R., and Cheatham, T. E. (2013) Ptraj and Cpptraj: Software for Processing and Analysis of Molecular Dynamics Trajectory Data. *J. Chem. Theory Comput. 9*, 3084−3095.
(33) Humphrey, W., Dalke, A., and Schulten, K. (1996) Vmd: Visual Molecular Dynamics. *J. Mol. Graphics 14*, 27−38.
(34) Classen, S., Hura, G. L., Holton, J. M., Rambo, R. P., Rodic, I., McGuire, P. J., Dyer, K., Hammel, M., Meigs, G., Frankel, K. A., and Tainer, J. A. (2013) Implementation and Performance of Sibyls: A Dual Endstation Small-Angle X-Ray Scattering and Macromolecular Crystallography Beamline at the Advanced Light Source. *J. Appl. Crystallogr. 46*, 1−13.
(35) Rambo, R. P., and Tainer, J. A. (2013) Accurate Assessment of Mass, Models and Resolution by Small-Angle Scattering. *Nature 496*, 477−481.
(36) Schneidman-Duhovny, D., Hammel, M., Tainer, J. A., and Sali, A. (2016) Foxs, Foxsdock and Multifoxs: Single-State and Multi-State Structural Modeling of Proteins and Their Complexes Based on Saxs Profiles. *Nucleic Acids Res. 44*, W424−429.
(37) Schneidman-Duhovny, D., Hammel, M., Tainer, J. A., and Sali, A. (2013) Accurate Saxs Profile Computation and Its Assessment by Contrast Variation Experiments. *Biophys. J. 105*, 962−974.
(38) Carter, L., Kim, S. J., Schneidman-Duhovny, D., Stohr, J., Poncet-Montange, G., Weiss, T. M., Tsuruta, H., Prusiner, S. B., and Sali, A. (2015) Prion Protein-Antibody Complexes Characterized by Chromatography-Coupled Small-Angle X-Ray Scattering. *Biophys. J. 109*, 793−805.
(39) Stratikos, E. (2014) Regulating Adaptive Immune Responses Using Small Molecule Modulators of Aminopeptidases That Process Antigenic Peptides. *Curr. Opin. Chem. Biol. 23*, 1−7.
(40) Zervoudi, E., Saridakis, E., Birtley, J. R., Seregin, S. S., Reeves, E., Kokkala, P., Aldhamen, Y. A., Amalfitano, A., Mavridis, I. M., James, E., Georgiadis, D., and Stratikos, E. (2013) Rationally Designed Inhibitor Targeting Antigen-Trimming Aminopeptidases Enhances Antigen Presentation and Cytotoxic T-Cell Responses. *Proc. Natl. Acad. Sci. U. S. A. 110*, 19890−19895.
(41) Evnouchidou, I., Momburg, F., Papakyriakou, A., Chroni, A., Leondiadis, L., Chang, S. C., Goldberg, A. L., and Stratikos, E. (2008) The Internal Sequence of the Peptide-Substrate Determines Its N-Terminus Trimming by Erap1. *PLoS One 3*, e3658.
(42) Zervoudi, E., Papakyriakou, A., Georgiadou, D., Evnouchidou, I., Gajda, A., Poreba, M., Salvesen, G. S., Drag, M., Hattori, A., Swevers,

DOI: 10.1021/acs.biochem.6b01170
Biochemistry XXXX, XXX, XXX−XXX

L., Vourloumis, D., and Stratikos, E. (2011) Probing the S1 Specificity Pocket of the Aminopeptidases That Generate Antigenic Peptides. *Biochem. J. 435*, 411−420.
(43) Mpakali, A., Saridakis, E., Harlos, K., Zhao, Y., Papakyriakou, A., Kokkala, P., Georgiadis, D., and Stratikos, E. (2015) Crystal Structure of Insulin-Regulated Aminopeptidase with Bound Substrate Analogue Provides Insight on Antigenic Epitope Precursor Recognition and Processing. *J. Immunol. 195*, 2842−2851.
(44) Mpakali, A., Giastas, P., Mathioudakis, N., Mavridis, I. M., Saridakis, E., and Stratikos, E. (2015) Structural Basis for Antigenic Peptide Recognition and Processing by Endoplasmic Reticulum (Er) Aminopeptidase 2. *J. Biol. Chem. 290*, 26021−26032.
(45) Papakyriakou, A., Zervoudi, E., Tsoukalidou, S., Mauvais, F. X., Sfyroera, G., Mastellos, D. C., van Endert, P., Theodorakis, E. A., Vourloumis, D., and Stratikos, E. (2015) 3,4-Diaminobenzoic Acid Derivatives as Inhibitors of the Oxytocinase Subfamily of M1 Aminopeptidases with Immune-Regulating Properties. *J. Med. Chem. 58*, 1524−1543.
(46) Chen, H., Li, L., Weimershaus, M., Evnouchidou, I., van Endert, P., and Bouvier, M. (2016) ERAP1-ERAP2 Dimers Trim MHC I-Bound Precursor Peptides; Implications for Understanding Peptide Editing. *Sci. Rep. 6*, 28902.
(47) Kanaseki, T., Blanchard, N., Hammer, G. E., Gonzalez, F., and Shastri, N. (2006) ERAAP Synergizes with Mhc Class I Molecules to Make the Final Cut in the Antigenic Peptide Precursors in the Endoplasmic Reticulum. *Immunity 25*, 795−806.
(48) Infantes, S., Samino, Y., Lorente, E., Jimenez, M., Garcia, R., Del Val, M., and Lopez, D. (2010) Cutting Edge: H-2l(D) Class I Molecule Protects an HIV N-Extended Epitope from in Vitro Trimming by Endoplasmic Reticulum Aminopeptidase Associated with Antigen Processing. *J. Immunol. 184*, 3351−3355.

DOI: 10.1021/acs.biochem.6b01170
Biochemistry XXXX, XXX, XXX−XXX